Article

Fibrous Structure and Stiffness of Designer Protein Hydrogels Synergize to Regulate Endothelial Differentiation of Bone Marrow Mesenchymal Stem Cells

Kai-Kai Tian, Sheng-Chen Huang, Xiao-Xia Xia, and Zhi-Gang Qian*

Read Online

ACCESS | Metrics & More | Article Recommendations | Supporting Information

ABSTRACT: Matrix stiffness and fibrous structure provided by the native extracellular matrix have been increasingly appreciated as important cues in regulating cell behaviors. Recapitulating these physical cues for cell fate regulation remains a challenge due to the inherent difficulties in making mimetic hydrogels with well-defined compositions, tunable stiffness, and structures. Here, we present two series of fibrous and porous hydrogels with tunable stiffness based on genetically engineered resilin-silk-like and resilin-like protein polymers. Using these hydrogels as substrates, the mechanoresponses of bone marrow mesenchymal stem cells to stiffness and fibrous structure were systematically studied. For both hydrogel series, increasing compression modulus from 8.5 to 14.5 and 23 kPa consistently promoted cell proliferation and differentiation. Nonetheless, the promoting effects were more pronounced on the fibrous gels than their porous counterparts at all three stiffness levels. More interestingly, even the softest fibrous gel (8.5 kPa) allowed the stem cells to exhibit higher endothelial differentiation capability than the toughest porous gel (23 kPa). The predominant role of fibrous structure on the synergistic regulation of endothelial differentiation was further explored. It was found that the stiffness signal activated Yes-associated protein (YAP), the main regulator of endothelial differentiation, via spreading of focal adhesions, whereas fibrous structure reinforced YAP activation by promoting the maturation of focal adhesions and associated F-actin alignment. Therefore, our results shed light on the interplay of physical cues in regulating stem cells and may guide the fabrication of designer proteinaceous matrices toward regenerative medicine.
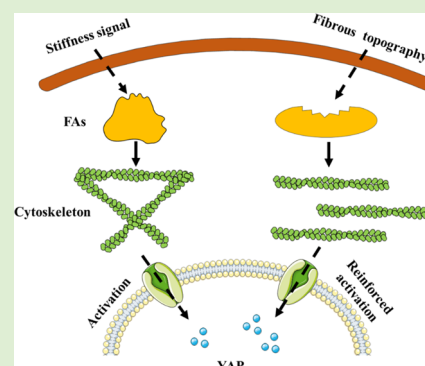
INTRODUCTION

The native extracellular matrix (ECM) is a highly complex fibrous network with tunable rigidity and micro/nanohierarchical structures. It could not only serve as a stable scaffold for cell organization but also provide a versatile microenvironment with controllable biophysical and biochemical cues for regulating stem cell behaviors and functions.[1−3] Increasing evidence indicates that the cellular response to environment signaling goes far beyond the biochemical cues.[4−6] Biophysical signals from ECM, especially matrix stiffness and topography, have gradually been recognized as key factors in regulating versatile cellular behaviors ranging from cell adhesion to differentiation.[7−10]

During the past decades, many efforts have been devoted to the recapitulation of the role of matrix stiffness in regulating cellular behaviors and functions using various materials including hyaluronic acid,[11,12] alginate,[13] silk,[14] and gelatin.[15] By mediating the stiffness of the matrices, the cell spreading and proliferation rate were well controlled.[16−19] In addition, stem cell fate could also be guided by tuning matrix stiffness.[20,21] Evidence indicates that stiffness could not only induce differentiation of stem cells into various cell types,[22] such as neurons, osteoblasts, and endothelial cells, but also regulate the extent to which stem cells can differentiate into a specific cell type.[23] Particularly, the stiffness-driven signaling pathways were continuously revealed, and hence how stiffness manipulated the cell behaviors were gradually identified.[24−26] However, the above studies only emphasized the contributions of the matrix stiffness to cell fate but ignored the effects of matrix morphology.

The fibrous architecture of matrix has been recently recognized as a key element to regulate cell functions, such as proliferation,[27,28] spreading,[29,30] and differentiation.[31,32] Various natural or synthetic polymers, such as silk,[33] gelatin,[31] dextran,[34] polycaprolactone,[35] and poly(ether carbonate urethane) urea,[36] have been fabricated into diverse materials with micro/nanofiber topography to regulate cell behaviors. Despite the positive effects of these fibrous materials on cell regulation, whether the material stiffness had a role and synergistic effect remains unclear[32−36] because the fabrication of diverse topographical structures would simultaneously alter
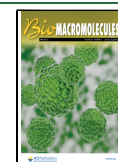
multiple material parameters including the stiffness.[37] Therefore, it is essential to design and fabricate ECM-mimic materials with fibrous structure and tunable stiffness for cell regulation studies.

Our group has been dedicated to studying how to fabricate diverse hydrogels with tunable stiffness and fibrous morphologies based on genetically engineered proteins.[38−40] Noticeably, recombinant resilin-like protein hydrogels have been broadly utilized in the field of tissue engineering due to their biocompatibility and tuning mechanical features.[41] Furthermore, resilin-like blocks as the intrinsically disordered structures could be further designed to contain the chimeric domain of silk-like blocks to fabricate diblock copolymers with tunable fibrillization morphologies, which may provide a feasible strategy to fabricate hydrogels with fibrous structures.[42]

Herein, the RGD-modified resilin-like (RGD-R32) and resilin-silk-like proteins (RGD-RS) were first designed and biosynthesized. These proteins were then cross-linked into porous or fibrous hydrogels with varying stiffness. Utilizing the fabricated protein hydrogels, we systematically investigated the effects of stiffness and fibrous structure in regulating bone marrow mesenchymal stem cells (BMSCs) proliferation, morphology, endothelial differentiation, and underlying mechanotransduction. We found that the fibrous topography and stiffness of these hydrogels synergized to drive mechanosensitive responses by rearranging cellular focal adhesions and morphologies. These results shed light on the interplay of the physical cues in manipulating cell behaviors and fate and provided a roadmap for designing biomimetic ECM to meet the need of tissue engineering and regenerative medicine.

■ MATERIALS AND METHODS

Construction of Expression Plasmids. Plasmids pET19b-R32 and pR4S8-5 were reported previously,[38,42] which allowed the expression of 32 repeats of the resilin-like sequence (GGRPSDSY-GAPGGGN) and 5 repeats of R4S8 [(GGRPSDSY-GAPGGGN)$_4$(GAGAGS)$_8$]. To meet the demand on cell culture, an inverse PCR was performed to introduce the Arg-Gly-ASP (RGD) cell-binding sequence to the aforementioned plasmids using primers RGD-forward (5′-CGTGGTGATATCGACGACGACGACAAG-3′) and RGD-reverse (5′-ATGGCCGCTGCTGTGATGATG-3′) by KOD-Plus-Mutagenesis Kit (TOYOBO, Osaka, Japan). The resulting constructs were identified by double digest with *Nde*I and *Bam*HI-HF and further confirmed by DNA sequencing. Plasmids pRGD-R32 and pRGD-R4S8-5 were thus obtained that encoded RGD-functionalized resilin-like protein (RGD-R32) and resilin-silk-like protein (RGD-RS), respectively, under transcriptional control of the strong T7 promoter.

Expression and Purification of Protein Polymers. The plasmids pRGD-R32 and pRGD-R4S8-5 were separately transformed to chemically competent *Escherichia coli* strain BL21(DE3) to express the protein polymers according to previously reported protocols.[39,42] Briefly, *E. coli* cells were sequentially cultured in Luria-Bertani (LB) and Terrific Broth (TB) medium containing 100 μg mL^{-1} ampicillin at 37 °C with 220 rpm shaking until the optical density at 600 nm (OD$_{600}$) reached 6−8 and then mixed with 0.1 mM isopropyl β-D-1-thiogalactoside (IPTG) at 16 °C for 12−14 h with 220 rpm shaking. The following steps including purification by Ni-NTA agarose resin affinity columns, dialysis in deionized water, and vacuum lyophilization were performed to harvest desired proteins. Protein purity was confirmed *via* 10% sodium dodecyl sulfate-polyacrylamide gel electrophoresis (SDS-PAGE), followed by densitometry analysis of the gel using ImageJ software (version Fiji, National Institutes of Health). The molecular weight of the protein was further identified by matrix-assisted laser desorption ionization time-of-flight (MALDI-TOF) mass spectrometry (Autoflex Speed; Bruker Daltonics, Leipzig, Germany).

Characterization of Protein Polymer Assemblies in Solution. Atomic force microscopy (AFM) images were captured in tapping mode using an Environment Control AFM System with a Nanonavi E-Sweep Model (SII Nano Technology Inc., Shizuoka, Japan). To prepare the specimens, the lyophilized proteins dissolved in Dulbecco's phosphate buffer solution (D-PBS, Sangon Biotech., Shanghai, China) at a concentration of 100 ng mL^{-1} were incubated at 37 °C for 0.5 h and then separately cast onto mica surfaces. Subsequently, the mica surfaces were rinsed with deionized water and air-dried. The specimens were then analyzed using a commercial silicon tip probe with the line-scan rate of 2 Hz for 2 μm by 2 μm scan regions. The acquired images were further processed by the NanoNavi II analysis software (SII Nano Technology Inc., Shizuoka, Japan).

Thioflavin-T (ThT)-staining experiment was conducted to characterize the formation of amyloid-like fibrils in protein solutions using Spark Multimode Microplate Reader (Tecan, Seestrasse, Switzerland). Ten microliters of protein solution at the specified concentrations were separately incubated at 37 °C for 0.5 h and then put into 100 μL of ThT solutions with a final concentration of 220 μg mL^{-1}. Equal volumes of D-PBS solutions were chosen to substitute protein solutions for background subtraction. Each sample was thoroughly mixed by pipetting up and down three times and transferred into a 96-well quartz plate. The fluorescence intensity was immediately collected on the plate reader by setting excitation and emission wavelengths to 440 and 480 nm, respectively.

Fabrication of Protein Hydrogels. The photochemical cross-linking strategy was adopted to fabricate RGD-R32 hydrogels. Protein solutions dissolved in D-PBS buffer with final concentrations of 8, 10, and 12% w/v, respectively, were incubated at 37 °C for 0.5 h and then mixed with [Ru(bpy)$_3$]$^{2+}$ (final concentration of 0.1 mM) and ammonium persulfate solutions (final concentration of 10 mM) for irradiation for 5 min using a 200 W white-light source. The horseradish peroxidase (HRP)-catalyzed cross-linking strategy was adopted to fabricate RGD-RS hydrogels. Similarly, pre-incubated protein solutions at 37 °C for 0.5 h with final concentrations of 6, 8, and 10% w/v, respectively, were mixed with HRP (final enzyme activity of 600 U mL^{-1}) and hydrogen peroxide (final concentration of 0.03% w/w) for 5 min in a 37 °C incubator. Before use, all samples were rinsed with D-PBS solutions.

Mechanical Testing. The compression testing of the hydrogels was performed on an Instron 5944 testing machine fitted with a 10 N loading cell (Instron Corporation, Canton, U.K.) at room temperature with humidity of around 65%. The hydrogel specimens were prepared inside a cylindrical mold with 8 mm diameter and 3 mm height. All of the tests were conducted at a loading rate of 0.5 mm min^{-1} with a compressive strain of 20%. Compressive moduli were calculated from the slope of the linear elastic region derived from the compressive stress−strain curves.

Structural and Morphological Characterization. Fourier transform infrared spectroscopy (FTIR) was conducted on a Nicolet 6700 spectrometer (Thermo Fisher Scientific Inc., Waltham, MA) in the transmission mode. For the lyophilized gel samples, 64 scans were co-added in the wavenumber range of 400−4000 cm^{-1} at a resolution of 4 cm^{-1}. Amide I region ranging from 1600 to 1700 cm^{-1} was chosen to analyze the secondary structure of protein hydrogels. The morphological structures of protein hydrogels were characterized using a Hitachi S-3400N scanning electron microscope (Hitachi, Tokyo, Japan). Before imaging, lyophilized hydrogels were mounted on a copper plate and coated with gold using a Leica EM SCD050 device (Leica Microsystems GmbH, Wetzlar, Germany).

Cell Culture. Wistar rat bone marrow mesenchymal stem cells (BMSCs), purchased from the Cell Bank of Chinese Academy of Science, were cultured in the α-MEM containing 10% fetal bovine serum (FBS) and 1% streptomycin/penicillin from Gibco (Grand Island, NY) and placed in an incubator with a constant humidity at 37 °C and 5% CO$_2$ atmosphere. For endothelial differentiation,
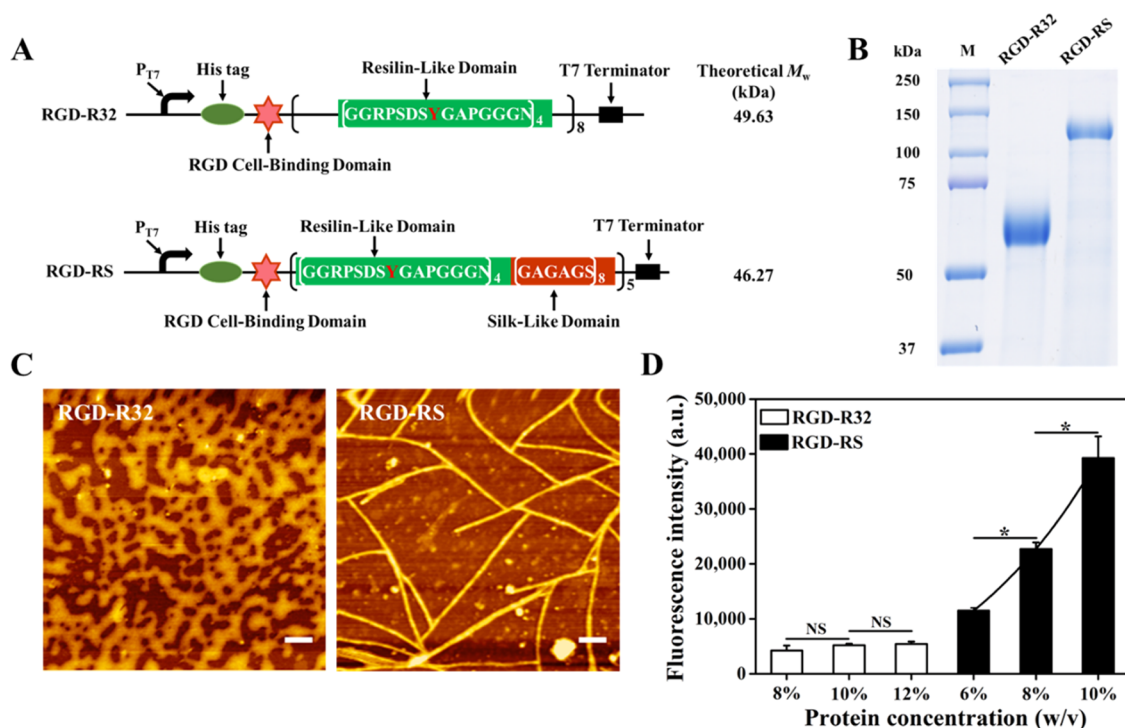
Figure 1. Biosynthesis and self-assembly of the recombinant protein polymers. (A) Genetic constructs of recombinant RGD-R32 and RGD-RS. (B) Ten percent SDS-PAGE analysis of the purified proteins. (C) Representative AFM images of amorphous aggregates from RGD-R32 and self-assembled nanofibers from RGD-RS upon incubation at 37 °C for 0.5 h. Scale bar: 200 nm. (D) ThT fluorescence assay of the proteins with varying concentrations upon incubation at 37 °C for 0.5 h. Data are derived from $n = 3$ biological replicates and presented as mean $\pm$ s.d. Statistical significance was determined using one-way ANOVA (NS, not significant with $p > 0.05$; $*p < 0.05$).

recombinant rat vascular endothelial growth factor 164 (VEGF164; Beyotime, Shanghai, China) at a final concentration of 50 ng mL^{-1} was added into the medium. The hydrogels for cell culture were prepared as described above in 48-well tissue culture plates (Thermo Fisher Scientific Inc., Waltham, MA) with 100 μL of premixed solutions, including pre-incubated protein solutions and various reactive reagents. Notably, all solutions were filtered using a 0.22 μm filter before mixing, and all hydrogels were soaked in α-MEM and sterilized under germicidal UV light for 1 day before seeding cells. Cells from passages 3−5 were used in all experiments. The culture medium was replaced every two days.

Cell Viability and Proliferation. To evaluate cell viability and proliferation, 20,000 cells were separately seeded on each hydrogel prepared in a 48-well tissue culture plate. For cell viability assay, BMSCs were cultured on hydrogels for three days and stained with Live/Dead Cell Imaging Kit (Thermo Fisher Scientific Inc., Waltham, MA) after rinsing with D-PBS three times. Ultrahigh-resolution confocal imaging of stained cell samples was performed using a Leica/TCS SP8 STED X3 confocal microscope (Leica Microsystems GmbH., Wetzlar, Germany) with 488 nm (green, live cells) and 570 nm (red, dead cells) excitation filters.

For cell proliferation testing, Cell Counting Kit-8 (CCK-8) assay was performed following the manufacturer's protocol (Beyotime, Shanghai, China). Briefly, the cells were separately cultured on different substrates for 1, 3, 5, and 7 days under standard conditions. At the appointed time, 200 μL of fresh medium and 20 μL of CCK-8 solutions were sequentially added to the rinsed cells with D-PBS and incubated for 2 h at 37 °C. Absorbance at 450 nm was then collected to analyze cell proliferation behavior using Spark Multimode Microplate Reader.

Immunofluorescence Assay. To evaluate the organization of the cell cytoskeleton, focal adhesion morphology, and YAP location, 10,000 cells were seeded on each hydrogel and cultured in α-MEM for 1 day at standard conditions. To evaluate the endothelial

differentiation, 20,000 cells were seeded on each hydrogel and cultured in a differential medium for 7, 14, and 21 days.

At the appointed time, BMSCs cultured on hydrogels were fixed with 4% paraformaldehyde (15 min), permeabilized with 0.1% Triton X-100 for 15 min, and then blocked for 30 min using the QuickBlock buffer (Beyotime, Shanghai, China) at room temperature. After that, the cells were incubated with the primary antibodies (diluted in blocking buffer) and fluorescein isothiocyanate (FITC) labeled phalloidin (Sigma-Aldrich, St. Louis, MO) for F-actin stain at the final concentration of 0.01 mg/mL overnight at 4 °C. After washing thoroughly with D-PBS, the cells were then stained with goat antimouse polyclonal secondary antibody (diluted in blocking buffer) for 1 h at room temperature. Before imaging, cell nuclei were counterstained with 4′,6-diamidino-2-phenylindole (DAPI) for 15 min at room temperature. Ultrahigh-resolution confocal imaging of stained samples was performed using a Leica/TCS SP8 STED X3 confocal microscope. All images were further processed using the ImageJ software. Notably, the mouse monoclonal antibody against CD31 (Abcam, Cambridge, U.K.) diluted to 1:100, mouse monoclonal antibody against vinculin (Proteintech Group Inc.) diluted to 1:50, and mouse monoclonal antibody against YAP (Proteintech Group Inc.) diluted to 1:100 were used to evaluate endothelial differentiation, focal adhesion morphology, and YAP location, respectively. FITC-conjugated secondary antibody (Proteintech Group Inc.) diluted to 1:10 was used for the analysis of CD31, and tetraethyl rhodamine isothiocyanate (TRITC) labeled secondary antibody (Proteintech Group Inc.) diluted to 1:50 was used for the analysis of focal adhesion and YAP.

Quantitative Image Processing. The cell alignment index was quantified by the kurtosis of angle distribution based on a two-dimensional fast Fourier transform (2D FFT) image analysis.[43] Briefly, the fluorescent cell images were converted to 8-bit grayscale and then cropped with the 1024 × 1024 pixel mask to reduce edge effects. The processed images were then subjected to 2D FFT analysis *via* ImageJ software to determine the pixel intensity distribution along
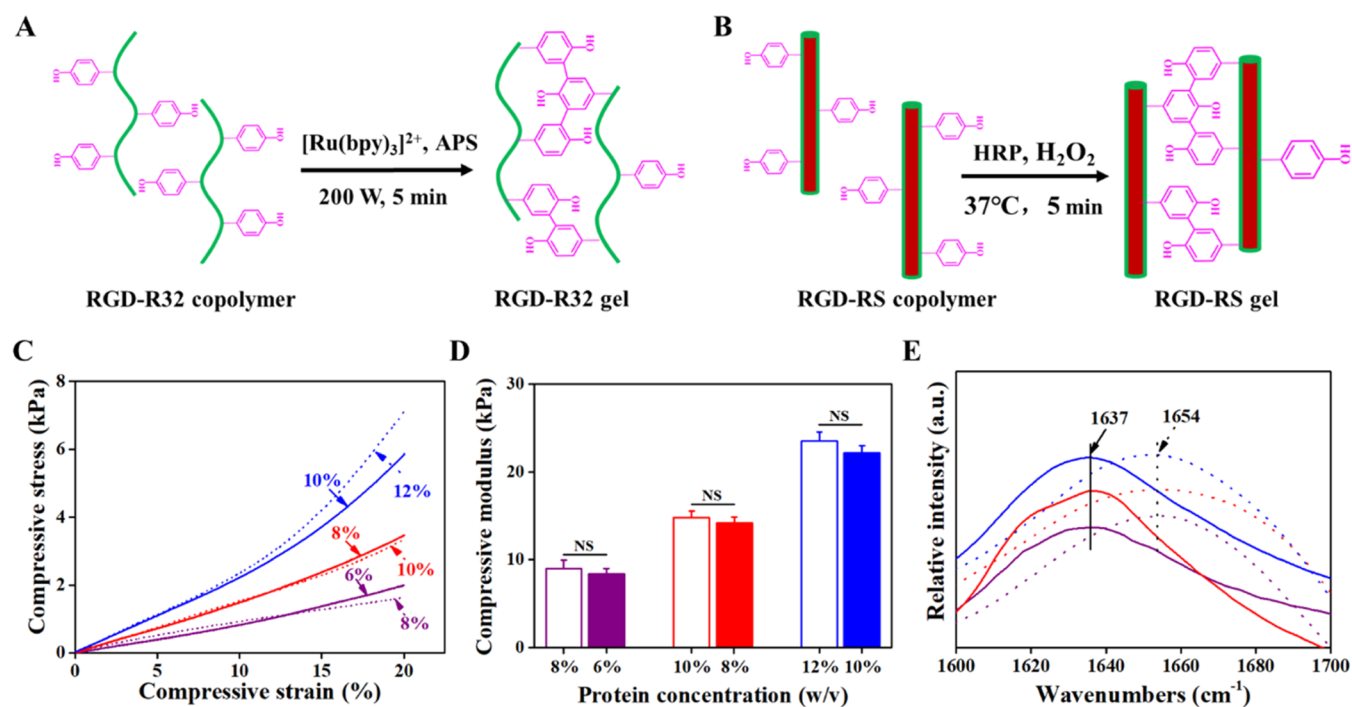
Figure 2. Fabrication and characterization of the protein hydrogels. Schematic illustration of (A) photo-induced cross-linking to fabricate RGD-R32 hydrogels and (B) HRP-catalyzed cross-linking to fabricate RGD-RS hydrogels. (C) Representative stress−strain curves of the hydrogels under 20% axial compressive load at the strain rate of 0.5 mm min^{-1}. The dotted and solid lines represent the RGD-R32 and RGD-RS hydrogels derived from precursor solutions with the indicated protein concentrations. (D) Compressive modulus of the hydrogels calculated from the linear region (10% strain) of each stress−strain curve. The open and solid bars represent the RGD-R32 and RGD-RS hydrogels, respectively. (E) Amide I regions of the FTIR spectra of the hydrogels described in panel C. Data are derived from $n = 3$ biological replicates and presented as mean ± s.d. Statistical significance was determined using one-way ANOVA (NS, not significant with $p > 0.05$).
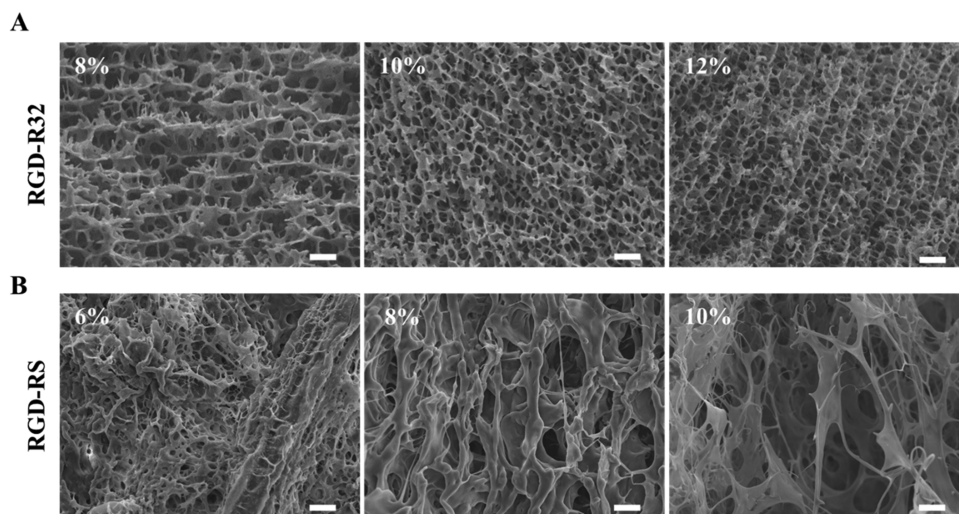
Figure 3. Cross-sectional SEM images of the lyophilized RGD-R32 (A) and RGD-RS (B) hydrogels fabricated from different concentrations of pre-incubated protein solutions at 37 °C for 0.5 h. Scale bar: 10 μm. Data are representative of five independent experiments.

the radian. The alignment index was defined as the fraction of actin fibers that were aligned within 20° of the peak angle, and this was normalized to the fraction of randomly oriented fibers that would lie within this range. A randomly aligned matrix would have an alignment index of 1, and the higher the value, the higher the fraction of actin fibers aligned near the peak angle.

An online Focal Adhesion Analysis Server was used to quantify the FA area and elongation index per cell according to the protocol.[44] The FA elongation index was quantified according to the following formula: FA elongation = major axis length/minor axis length.

To evaluate the YAP nuclear location of cells, the nucleus-to-cytosol intensity ratio was calculated according to the following formula: intensity ratio (nuc/cyt) = I_{nuc}/I_{cyt}, where I_{nuc} and I_{cyt} represent the intensity values of the pixels inside the nucleus and just outside the nucleus region with the same area.

Quantitative Real-Time PCR (qPCR) Analysis. Twenty thousand cells were seeded on each hydrogel and cultured for 7, 14, and 21 days using the differential medium. At the appointed time, the total RNA was extracted using a HiPure Total RNA Micro Kit (Angen Biotech Co., Ltd., Guangzhou, China) following the manufacturer's protocol. Complementary DNA (cDNA) was
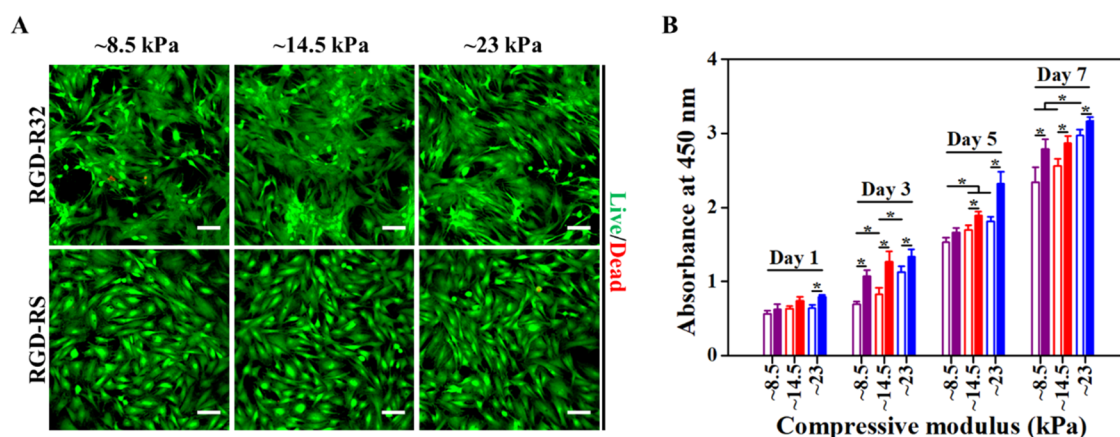
Figure 4. Viability and proliferation of the BMSCs. (A) Confocal images of the BMSCs cultured for 3 days on the RGD-R32 and RGD-RS hydrogels with three stiffness levels by Live (green)/Dead (red) staining. Scale bar: 100 μm. (B) Proliferation of BMSCs on the RGD-R32 (open bars) and RGD-RS hydrogels (solid bars) with three stiffness levels evaluated by CCK-8 assay within 7 days. Data in (A) are representative of $n = 5$ biological replicates. Data in (B) are derived from $n = 5$ biological replicates and presented as mean $\pm$ s.d. Statistical significance was determined using one-way ANOVA (*$p < 0.05$).
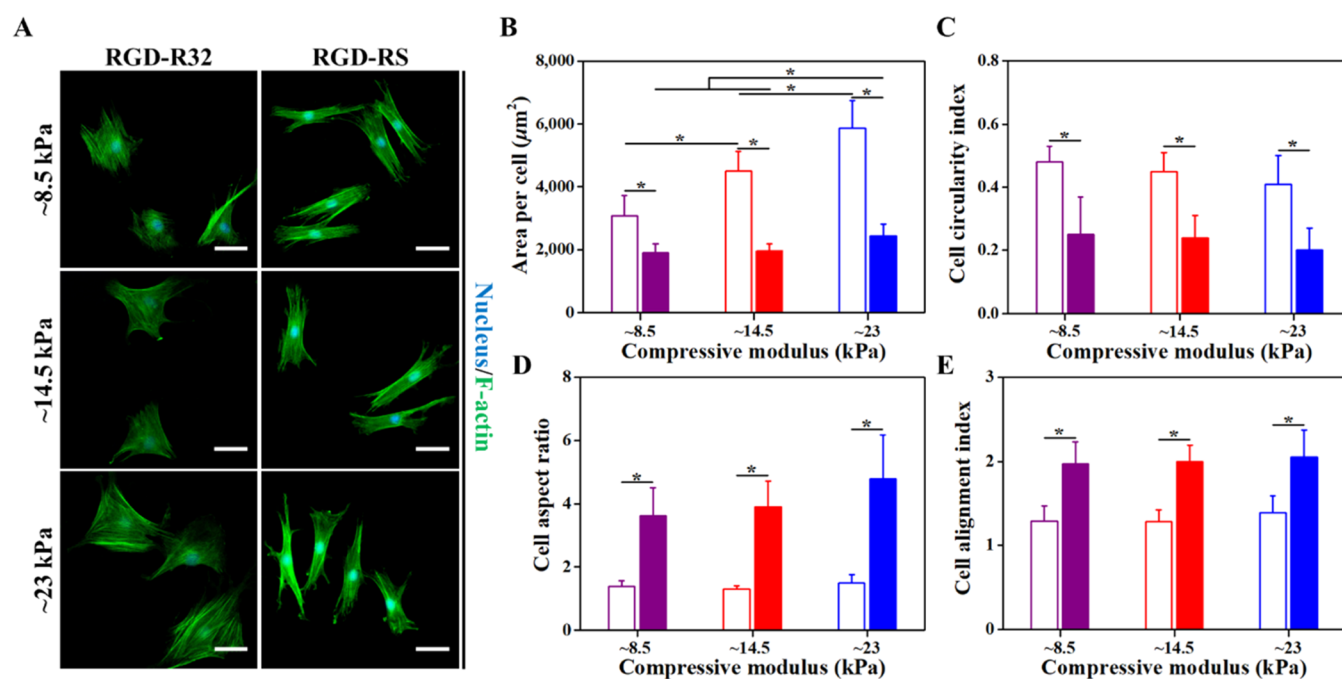

Figure 5. Effects of fibrous structure and stiffness of the protein hydrogels on the morphology of BMSCs. (A) Representative confocal images of the BMSCs stained with Phalloidine-FITC (actin, green) and DAPI (nuclei, blue). The cells were cultured on the hydrogels for 1 day and stained before imaging. Scale bar: 50 μm. Quantification of spreading area (B), circularity index (C), aspect ratio (D), and alignment index (E) of the BMSCs. The open and solid bars represent the cells cultured on the respective RGD-R32 and RGD-RS gels. Data in (A) are representative of $n = 6$ biological replicates. Data in (B)−(E) are derived from $n = 6$ biological replicates (over 500 single cells) and presented as mean $\pm$ s.d. Statistical significance was determined using one-way ANOVA (*$p < 0.05$).

synthesized using a RevertAid First Strand cDNA Synthesis Kit (Thermo Fisher Scientific, Waltham, MA). qPCR analysis was performed using a qTOWER3G touch system (Analytik Jena AG, Jena, Germany) loaded with mixtures of the Luna Universal qPCR Master Mix (New England Biolabs Inc., Ipswich, MA), template DNA, and specific primers. The primers used for housekeeping gene glyceraldehyde 3-phosphate dehydrogenase (GAPDH) were GAPDH-forward (5′-AACTTGCCGTGGGTAGAGTC-3′) and GAPDH-reverse (5′-AACTTGCCGTGGGTAGAGTC-3′). The primers used for the targeted CD31 gene were CD31-forward (5′-GGACTGCGCCCATCACTTACC-3′) and CD31-reverse (5′-TCATCCACCGGGGGCTATTACCTT-3′). The relative fold gene expression of CD31 was calculated using a relative quantitative

method (the $2^{(-\triangle\triangle Ct)}$ method), with normalization to the housekeeping gene glyceraldehyde 3-phosphate dehydrogenase (GAPDH) and calibration to the sample with the highest $\triangle Ct$-value.

Western Blot Analysis. Twenty thousand cells were seeded on each hydrogel and cultured for 14 days using the differential medium. The cells were lysed using a RIPA lysis buffer containing 1 mM phenylmethanesulfonyl fluoride (Beyotime) following the manufacturer's protocols. Total proteins were collected and quantified using a BCA kit (Thermo Fisher Scientific Inc., Waltham, MA). Proteins were separated in 10% SDS-PAGE, followed by the transfer to polyvinylidene fluoride (PVDF) membrane. The PVDF membranes were blocked using the QuickBlock buffer (Beyotime) for 30 min at room temperature and incubated with mouse monoclonal antibody
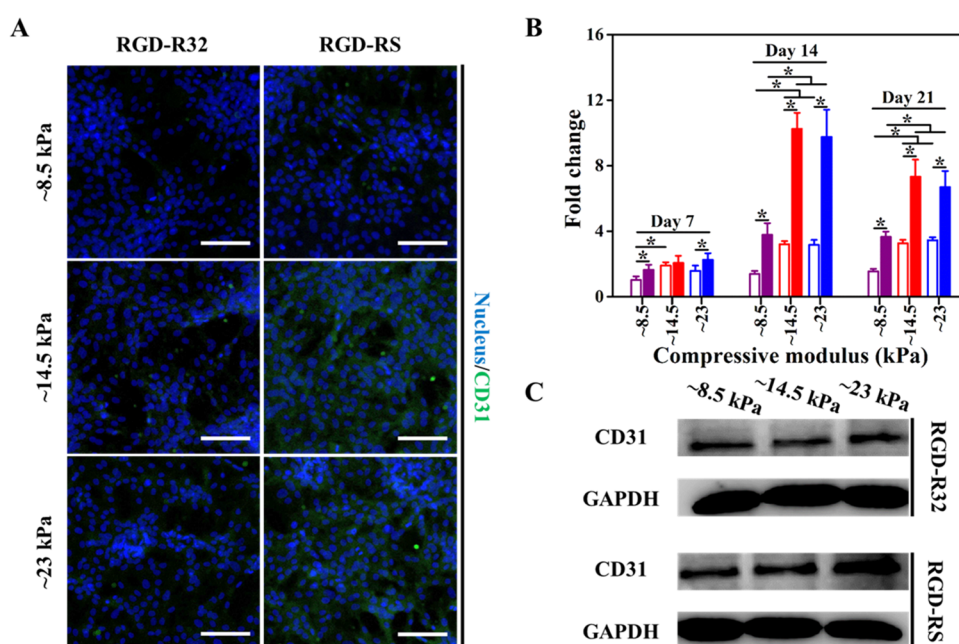
Figure 6. Effects of fibrous morphology and stiffness on the endothelial differentiation of the BMSCs cultured in the medium with VEGF. (A) Confocal imaging of the cells cultured for 14 days and immuno-stained for testing CD31 expression (green). The nuclei were stained with DAPI (blue). Scale bar: 100 μm. (B) Relative CD31 gene expression levels from the cells cultured on the RGD-R32 (open bars) and RGD-RS (solid bars) gels on days 7, 14, and 21. The fold change values were calculated relative to the cells cultured on the ~8.5 kPa RGD-R32 gel on day 7. (C) Western blot analysis of the CD31 protein in the cultured cells on day 14. Data in (A) are representative of $n = 6$ biological replicates, and data in (B) are derived from $n = 3$ biological replicates and presented as mean $\pm$ s.d. Data in (B) and (C) are representative of three independent experiments. Statistical significance was determined using one-way ANOVA (*$p < 0.05$).
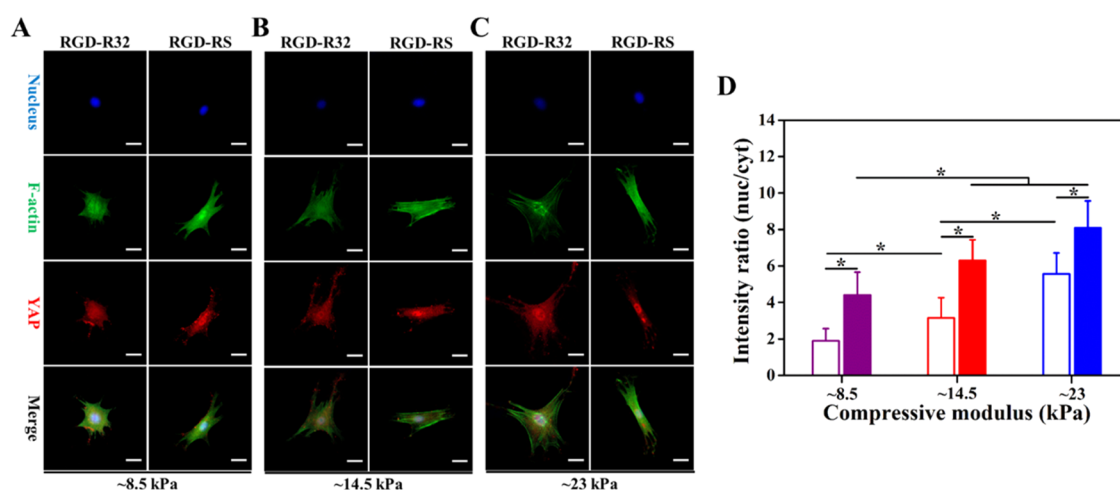
Figure 7. Effects of fibrous morphology and stiffness of the protein hydrogels on YAP nuclear localization. (A)−(C) Immunofluorescence labeling and confocal images of YAP (red) with nucleus (blue) and F-actin (green) counterstain for the BMSCs cultured on the gels with varying stiffnesses. Scale bar: 25 μm. (D) Quantification of the ratio of the fluorescence intensity of nuclear YAP to that in the cytosol (nuc/cyt). The open and solid bars represent the cells cultured on the RGD-R32 and RGD-RS hydrogels, respectively. Data in (A)−(C) are representative of $n = 8$ biological replicates. Data in (D) are derived from $n = 8$ biological replicates (over 600 single cells) and presented as mean $\pm$ s.d. Statistical significance was determined using one-way ANOVA (*$p < 0.05$).

against CD31 (Abcam, Cambridge, U.K.) diluted to 1:200 in blocking buffer or a mouse monoclonal antibody against GAPDH (Proteintech Group, Inc.) diluted to 1:1000 in blocking buffer at 4 °C overnight, followed by HRP-linked horse antimouse secondary antibody (Proteintech Group, Inc., Philly, PA) diluted to 1:2000 in blocking buffer for 1 h at room temperature. Autoradiography was performed to detect the band of CD31 protein using the BeyoECL Moon Kit (Beyotime).

Statistical Analysis. All data were derived from at least three biological replicates and presented as mean $\pm$ s.d. Statistical differences were analyzed using a one-way analysis of variance (ANOVA), and a p-value less than 0.05 indicated statistical significance.

RESULTS AND DISCUSSION

Biosynthesis and Characterization of Recombinant Protein Polymers. To design materials suitable for cell cultures, an Arg-Gly-ASP (RGD) cell-binding domain was genetically fused to N terminus of protein polymer R32
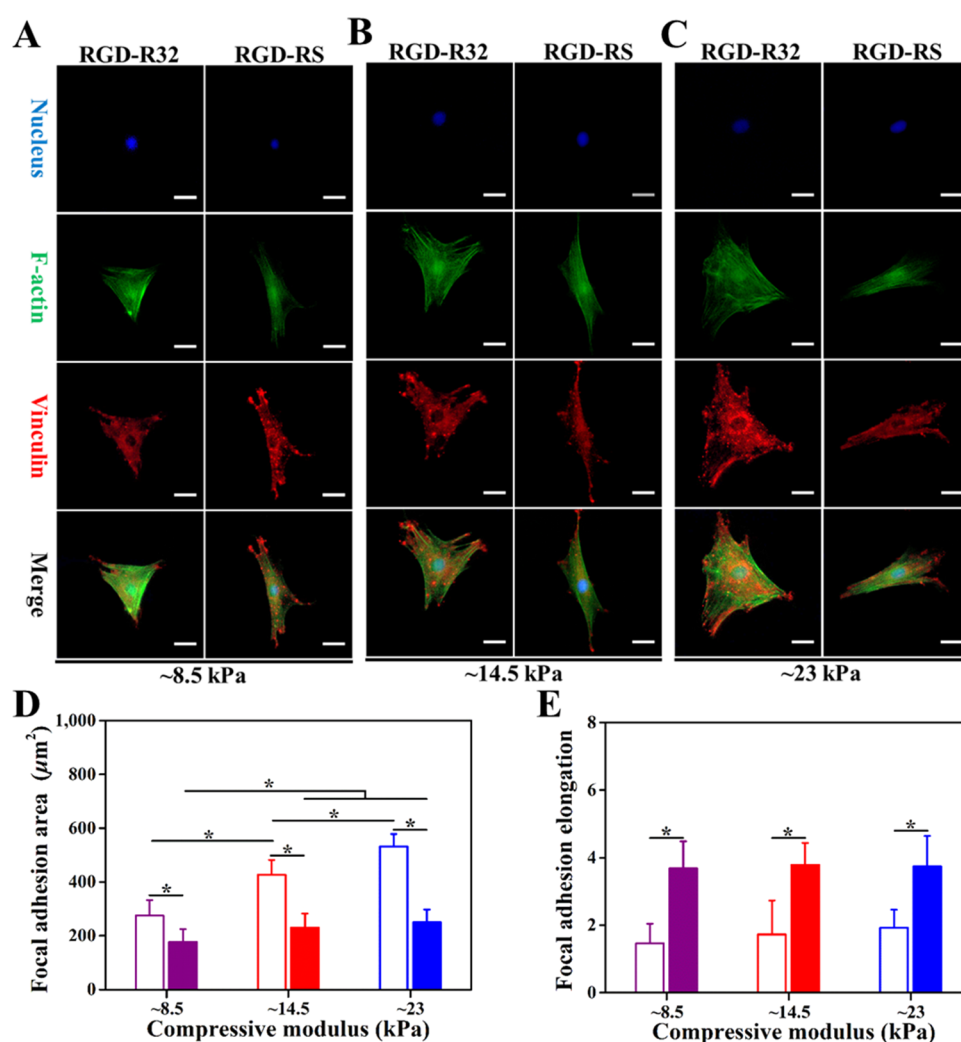
Figure 8. Effects of fibrous morphology and stiffness of the protein hydrogels on focal adhesion. (A)−(C) Immunofluorescence labeling and confocal images of vinculin (red) with nucleus (blue) and F-actin (green) counterstain for the cells cultured on the gels with varying stiffnesses. Scale bar: 25 μm. (D) Focal adhesion area and (E) elongation index of the cells cultured on the respective RGD-R32 (open bars) and RGD-RS (solid bars) gels. Data in (A)−(C) are representative of $n = 8$ biological replicates. Data in (D) and (E) are derived from $n = 8$ biological replicates (over 500 single cells) and presented as mean ± s.d. Statistical significance was determined using one-way ANOVA (*$p < 0.05$).

containing 32 repeats of the resilin-like sequence (GGRPSDSYGAPGGGN) and RS containing 5 repeats of R4S8 [(GGRPSDSYGAPGGGN)$_4$(GAGAGS)$_8$], respectively, termed as RGD-R32 and RGD-RS (Figure 1A). These two proteins were expressed in the host cell *E. coli* BL21 (DE3) and purified using Ni-chelating affinity chromatography. SDS-PAGE analysis revealed that the purity of both proteins reached more than 90% (Figure 1B). However, aberrant gel mobility was consistently observed, which might be due to the intrinsically disordered structures of target proteins. Thus, we further identified the proteins by MALDI-TOF MS, which proved that the molecular weights of RGD-R32 and RGD-RS proteins were 49,747.57 and 46,144.93 Da (Figure S1), consistent with their theoretical molecular weights as shown in Figure 1A. The yields of purified RGD-R32 and RGD-RS proteins were approximately 45 and 75 mg L^{-1}, respectively, of bacterial culture in shake flasks.

Resilin-silk copolymers (RS) were reported to have the capability of self-assembly into fibrillar structures.[42] To identify whether the RGD-functionalized RS proteins still have the ability, AFM imaging was performed. As shown in Figure 1C,

the RGD-RS protein could form uniform nanofibers exceeding several micrometers in length and 28 ± 6 nm in diameter with incubation at 37 °C for 0.5 h, which proved that incorporated RGD did not interfere with the assembly of RS proteins. On the contrary, the RGD-R32 protein could only form amorphous aggregates, which was consistent with our previous findings on the R32 protein.[39] To quantify the fibrillar structures of the RGD-RS protein at different concentrations, the ThT fluorescence assay was performed. Interestingly, the ThT fluorescence intensity of RGD-RS almost linearly increased with protein concentrations while no changes were observed for RGD-R32, suggesting that the formation of RGD-RS fibrils profited from the β-sheet formation and was concentration-dependent (Figure 1D). Taken together, two types of protein polymers with and without fibrillar assembly capability have been successfully synthesized.

Preparation and Characterization of Recombinant Protein Hydrogels. To fabricate the RGD-R32 and RGD-RS protein hydrogels with comparable mechanical features and suitable for endothelial differentiation, dityrosine cross-linking methods catalyzed by ruthenium (Figure 2A) or horseradish
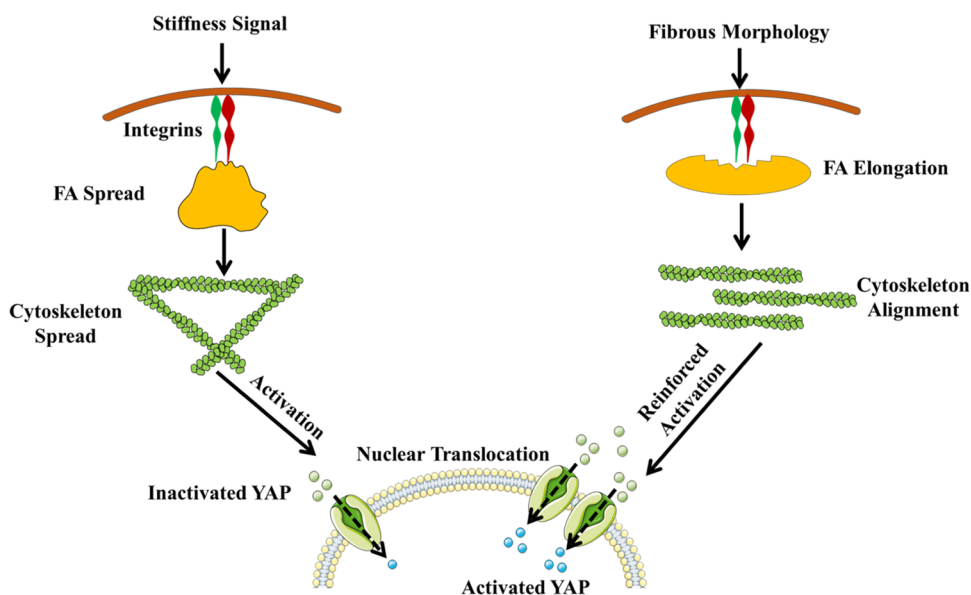
Figure 9. Schematic illustration of the influences of fibrous structure and stiffness on the endothelial differentiation of BMSCs. Compared with the effect of stiffness signals on YAP activation *via* focal adhesion and F-actin spreading, a fibrous structure reinforces YAP activation by inducing focal adhesion elongation and F-actin orientation, resulting in enhanced endothelial differentiation capacity of BMSCs.

peroxidase (Figure 2B) were used to cross-link different concentrations (6−12% w/v) of RGD-R32 and RGD-RS proteins, respectively. The mechanical properties of these gels were then determined by compression tests. According to the stress−strain curves (Figure 2C), the compressive modulus (defined as the slope of a uniaxial stress−strain curve, indicative of the gel stiffness) was elevated with an increase in the precursor protein concentration for both series of the hydrogels. Notably, similar compressive moduli were obtained between each group for RGD-R32-8% and RGD-RS-6%, RGD-R32-10% and RGD-RS-8%, and RGD-R32-12% and RGD-RS-10%, which were respectively ∼8.5, ∼14.5, and ∼23 kPa (Figure 2D), covering suitable stiffness for endothelial differentiation.[20,21,45]

To understand the conformational structures of the hydrogels, FTIR analysis was performed. As shown in Figure 2E, RGD-R32 hydrogels showed a major peak at ∼1654 cm^{-1}, indicating the existence of predominant random coils. In contrast, a major peak at ∼1637 cm^{-1} was observed for the RGD-RS gels, suggestive of the formation of β-sheet structures, which might be attributed to the fibrillar aggregations of silk-like blocks.

To further identify the internal morphologies of the hydrogels, SEM analysis was performed. The acquired images showed that all of the RGD-R32 hydrogels exhibited homogeneous porous structures, and the pore sizes decreased as the concentration of protein increased (Figure 3A), while the RGD-RS hydrogels exhibited fibrous network structures at both nano- and microscales, which were also adjustable by the protein concentrations (Figure 3B).

Notably, the tripeptide RGD originally identified within fibronectin is an important biochemical motif that mediates cell attachment to the matrix.[4] With this in mind, we attempt to fabricate the two series of RGD-tagged protein hydrogels at three stiffness levels yet with the same protein concentration. In spite of many attempts, we can only achieve a dissimilar and limited stiffness range for the porous RGD-R32 and fibrous RGD-RS hydrogels, which are not suitable for use in studying

proliferation and endothelial differentiation of the BMSCs. This reflects the daunting challenge in making mimetic hydrogels with well-defined compositions, tunable stiffness, and structures.[37] Therefore, we finally choose to vary the precursor protein concentrations to tune the stiffness of the resulting hydrogels and minimize the RGD concentration gap between groups so that uncovering the predominant roles of matrix structure and stiffness in cell culture is possible.

Viability and Proliferation of BMSCs on Protein Hydrogels. The cytocompatibility of the RGD-R32 and RGD-RS hydrogels was first evaluated *via* the Live/Dead assay using the bone marrow mesenchymal stem cells (BMSCs). Confocal images showed that BMSCs could attach and spread on both series of hydrogels, and almost no dead cells were detected (Figure 4A), indicating the excellent cytocompatibility of those gels. Next, the cell proliferation on both series of hydrogels was evaluated *via* the CCK-8 assay. Results showed that BMSCs could proliferate well on both hydrogels with stiffness ranging from ∼8.5 to 23 kPa, and the stiffer hydrogels resulted in a higher proliferation rate of cells over the course of 7 days (Figure 4B), which is consistent with earlier studies.[46] More interestingly, the fibrous hydrogels were more beneficial for cell proliferation than their porous counterparts, revealing the important role of fibrous topography. This result seems contradictory to the previous finding that the formation of β-sheets suppressed cell proliferation.[26,47] The fibrous structures of β-sheets could provide a preferable cue to promote cell proliferation.

Effects of Mechanical and Structural Cues on the Morphology of BMSCs. It is well known that cell morphology, such as spreading area, shape factor, and aspect ratio, plays an important role in regulating the differentiation of stem cells. We next tested the influences of substrate structures and stiffness on the cell morphology of BMSCs. Confocal images showed that the cells exhibited flattened and irregular shapes on porous RGD-R32 hydrogels with varying stiffness, whereas narrow and elongated shapes were observed on fibrous RGD-RS hydrogels (Figure 5A), which were similar to

in vivo cell morphology. Quantitative results showed that the spreading area on porous hydrogels increased significantly with an increase in substrate stiffness, whereas on fibrous hydrogels, changes were not so significant (Figure 5B). Notably, the spreading areas on porous hydrogels were consistently larger than that on fibrous hydrogels within the tested range of substrate stiffness, which suggested that the fibrous structure might restrict the cell spreading. To further quantify cell morphology, circularity index (C_{CI}) and aspect ratio (AR) were also analyzed. C_{CI} represents the degree of similarity to a circumference with a value ranging from 0 to 1 (perfect circle), and C_{AR} represents solely the degree of elongation. Analytical results showed that the cells cultured on the fibrous hydrogels had significantly lower C_{CI} (~0.21) and higher C_{AR} (~4) than those on the porous gels, which indicated that the fibrous structure guided the BMSCs to form an elongated morphology (Figure 5B,C).

The cytoskeleton is an essential modulator of cell morphology; therefore, the actin organization of BMSCs was then investigated. Typical confocal fluorescence images of BMSCs stained with phalloidin-FITC (actin, green) and DAPI (nuclei, blue) are shown as Figure S2A and converted into a fast Fourier transform (FFT)-based image for cell orientation analysis (Figure S2B).[43,48] Obviously, the alignment indexes for cells on the fibrous hydrogels with three stiffness levels were consistently higher than that on the porous gels (Figure 5D), indicating a well-oriented organization of actin cytoskeleton. In summary, the fibrous structure of RGD-RS hydrogels guided the BMSCs to form an *in vivo* like elongated cell morphology and rearrange their actin cytoskeleton, which might be beneficial for cell differentiation.

Effects of Mechanical and Structural Cues on the Endothelial Differentiation of BMSCs. To clarify the influences of substrate structures and stiffness on endothelial differentiation, the BMSCs were seeded on the RGD-R32 and RGD-RS hydrogels and cultured in the α-MEM medium with or without recombinant rat vascular endothelial growth factor 164 (VEGF164). The cell samples were periodically taken and fluorescently labeled for monitoring the expression of the CD31 protein, a characteristic marker expressed in endothelial cells. Confocal imaging revealed obvious CD31 expression for the cells cultured on the protein hydrogels with VEGF in the medium on day 14 (Figure 6A) and day 21 (Figure S3), indicating the occurrence of endothelial differentiation of the BMSCs. Notably, the expression of CD31 for the cells cultured on fibrous RGD-RS hydrogels was more significant than that on porous RGD-R32 hydrogels with similar stiffness. However, none of these hydrogels supported endothelial differentiation of the BMSCs in the culture medium without VEGF because expression of the marker protein CD31 was undetectable in this scenario (Figure S4). These results suggested that external addition of the differentiation factor was required for the fibrous protein hydrogels to promote endothelial differentiation of the BMSCs. Although recent studies have suggested that formation of endothelial tubes and endothelial sprouting from human umbilical vein endothelial cells could be promoted by DNA matrices without external differentiation factors,[49,50] our results are consistent with canonical findings that treatment with VEGF is linked to the differentiation of MSCs into vascular cell types and other lineages.[51,52]

To further explore the endothelial differentiation, the mRNA expression levels of the CD31 gene for various groups were quantified using qPCR analysis (Figure 6B). Results showed

that the expression of the CD31 gene reached the highest level on day 14 for cells cultured on both series of hydrogels. Therefore, we chose the data for day 14 for the following analysis. The expression levels of the CD31 gene on both hydrogels with moduli of ~14.5 and ~23 kPa, respectively, were comparable and around twofold higher than those on gels with the modulus of ~8.5 kPa, indicating that the appropriate stiffness of substrates was necessary for cell differentiation. Interestingly, the cells cultured on the fibrous hydrogels with three stiffness levels (~8.5, ~14.5, and ~23 kPa) had 2.73-, 3.18-, and 3.09-fold higher levels of CD31 expression, respectively, than that of their porous counterparts. In addition, the fibrous hydrogels with the lowest modulus (~8.5 kPa) promoted the cells to express even higher levels of CD31 than the porous gels with the highest modulus (~23 kPa), suggesting that fibrous structure could make up for the role of stiffness cues on cell differentiation and might be a more powerful one.

Western blot was next performed to quantify the protein level of CD31. Consistent with the mRNA expression results, the CD31 protein levels increased with the modulus of both series of hydrogels and the cells on RGD-RS fibrous hydrogels exhibited significantly higher levels of CD31 than their porous counterparts (Figures 6C and S5). These results further supported the fact that a fibrous structure might be a more powerful cue on cell differentiation.

YAP-Mediated Mechanotransduction Regulates Endothelial Differentiation. It is well documented that the endothelial differentiation of stem cells is mainly regulated by the activation of the Hippo transcriptional co-activator Yes-associated protein (YAP), which is expressed both in the nucleus as the transcriptional co-activator and cytoplasm as an inactive component due to phosphorylation.[53,54] As a rheostat to mediate stem cell behavior, inactive YAP in the cytoplasm is translocated into the nucleus to induce endothelial differentiation.[55] To investigate the influence of fibrous structure and mechanical features on YAP location, BMSCs were cultured on both series of hydrogels with varying stiffness. Confocal images showed that the fluorescently labeled YAP (red) was obviously enriched into the nucleus for cells on the fibrous hydrogels with varying stiffness, but only for cells on the porous hydrogels with stiffness reaching ~23 kPa (Figures 7A−C and S6).

Quantitative analysis revealed that YAP exhibited increased enrichment into the nucleus with increasing stiffness for both series of hydrogels and YAP nuclear localization (indicated by nucleus/cytoplasm ratio of YAP[56]) for cells on the fibrous hydrogels was significantly higher than that on the porous hydrogels (Figure 7D). Notably, YAP nuclear localization for cells on the fibrous hydrogels with a modulus of ~8.5 kPa was similar to that on the porous hydrogels with ~23 kPa modulus. These results proved that both structural and mechanical cues promote YAP activation and nuclear translocation, but a fibrous structure may be a more powerful signal to mediate YAP nuclear localization for endothelial differentiation.

Vinculin is a marker protein for focal adhesion, which is closely related to YAP nuclear localization.[57,58] Therefore, the cells were fluorescently labeled for vinculin protein to characterize the difference in focal adhesion formation on both RGD-R32 and RGD-RS hydrogels (Figures 8A−C and S7). Immunofluorescence confocal images showed that the majority of vinculin protein accumulated into clusters underlying plasma membrane of cells on RGD-R32 hydrogels,

whereas dash-like vinculin patches were observed at the tips of actin fibers on RGD-RS hydrogels. Quantitative analysis of focal adhesion was next performed by an online Focal Adhesion Analysis Server, which showed that the focal adhesion area on the porous hydrogels increased significantly with substrate stiffness and was much higher than that on the fibrous hydrogels (Figure 8D). This result complied with the above findings but was contrary to a previous report that a larger focal adhesion area led to a higher YAP nuclear localization.[57] Therefore, we further identified the maturity of focal adhesion by elongation index, which was another important factor affecting the YAP nuclear localization.[58,59] At the three stiffness levels, the elongation indexes of the cells on the fibrous hydrogels were 2.50-, 2.20-, and 1.95-fold higher than their porous counterparts (Figure 8E). This result indicated that a fibrous structure improved the YAP nuclear localization by promoting the maturity of focal adhesions instead of expanding the focal adhesion area.

Based on the above results, possible signaling pathways are summarized to clarify how fibrous structure and stiffness regulate the endothelial differentiation of BMSCs (Figure 9). Stiffness signals activated a translocation of YAPs into the nucleus by facilitating the spread of focal adhesion and actin fibers. However, the fibrous structure could reinforce the activation of YAP by promoting the elongation of focal adhesion and alignment of actin fibers. To the best of our knowledge, it is the first time to clarify the respective and synergistic roles of fibrous structure and stiffness signals in regulating endothelial differentiation.

■ CONCLUSIONS

To investigate the synergistic role of fibrous structure and stiffness in regulating cell behaviors, we designed and biosynthesized genetically engineered RGD-R32 and RGD-RS protein polymers. By tuning the concentration and self-assembling capability of protein solutions, we successfully fabricated two series of porous and fibrous hydrogels with varying and comparable stiffness. Utilizing the hydrogels as substrates for cell cultures, we observed that fibrous hydrogels favored a higher proliferation of BMSCs than their porous counterparts and induced BMSCs to form elongated and *in vivo* like morphologies. In addition, the fibrous hydrogels obviously enhanced the endothelial differentiation capacity of BMSCs, which were ascribed to the reinforced activation of YAP derived from the elongation of focal adhesion and alignment of actin fibers. Taken together, the results deepened our understanding of the synergetic effect of structural and mechanical cues on cell behaviors and may provide guidance for designing engineered biomaterials for tissue engineering.

■ ASSOCIATED CONTENT

ⓢ Supporting Information

The Supporting Information is available free of charge at https://pubs.acs.org/doi/10.1021/acs.biomac.2c00032.

Mass spectroscopy analyses of the purified proteins (Figure S1), effects of fibrous structure and stiffness on the alignment of the cytoskeleton of BMSCs (Figure S2), confocal images of the BMSCs cultured on the protein hydrogels in the medium with VEGF for testing the expression of the endothelial marker CD31 on days 7 and 21 (Figure S3), confocal images of the BMSCs cultured on the protein hydrogels without VEGF (Figure S4), quantification of the CD31 protein expression levels in the cultured BMSCs (Figure S5), imaging of YAP nuclear localization (Figure S6), and imaging of focal adhesion (Figure S7) (PDF)

■ AUTHOR INFORMATION

Corresponding Author

Zhi-Gang Qian − *State Key Laboratory of Microbial Metabolism, Joint International Research Laboratory of Metabolic & Developmental Sciences, and School of Life Sciences and Biotechnology, Shanghai Jiao Tong University, Shanghai 200240, People's Republic of China;* ⓞ orcid.org/0000-0002-0133-0605; Email: zgqian@sjtu.edu.cn

Authors

Kai-Kai Tian − *State Key Laboratory of Microbial Metabolism, Joint International Research Laboratory of Metabolic & Developmental Sciences, and School of Life Sciences and Biotechnology, Shanghai Jiao Tong University, Shanghai 200240, People's Republic of China*

Sheng-Chen Huang − *State Key Laboratory of Microbial Metabolism, Joint International Research Laboratory of Metabolic & Developmental Sciences, and School of Life Sciences and Biotechnology, Shanghai Jiao Tong University, Shanghai 200240, People's Republic of China*

Xiao-Xia Xia − *State Key Laboratory of Microbial Metabolism, Joint International Research Laboratory of Metabolic & Developmental Sciences, and School of Life Sciences and Biotechnology, Shanghai Jiao Tong University, Shanghai 200240, People's Republic of China;* ⓞ orcid.org/0000-0001-8375-1616

Complete contact information is available at:
https://pubs.acs.org/10.1021/acs.biomac.2c00032

Notes

The authors declare no competing financial interest.

■ REFERENCES

(1) Xu, Y.; Shi, G. D.; Tang, J. C.; Cheng, R. Y.; Shen, X. F.; Gu, Y.; Wu, L.; Xi, K.; Zhao, Y. H.; Cui, W. G.; Chen, L. ECM-Inspired Micro/Nanofibers for Modulating Cell Function and Tissue Generation. *Sci. Adv.* **2020**, *6*, No. eabc2036.

(2) Lutolf, M. P.; Gilbert, P. M.; Blau, H. M. Designing Materials to Direct Stem-Cell Fate. *Nature* **2009**, *462*, 433−441.

(3) Petridou, N. I.; Spiró, Z.; Heisenberg, C. P. Multiscale Force Sensing in Development. *Nat. Cell Biol.* **2017**, *19*, 581−588.

(4) Geiger, B.; Spatz, J. P.; Bershadsky, A. D. Environmental Sensing through Focal Adhesions. *Nat. Rev. Mol. Cell Biol.* **2009**, *10*, 21−33.

(5) Hou, Y.; Yu, L. X.; Xie, W. Y.; Camacho, L. C.; Zhang, M.; Chu, Z. Q.; Wei, Q.; Haag, R. Surface Roughness and Substrate Stiffness Synergize to Drive Cellular Mechanoresponse. *Nano Lett.* **2020**, *20*, 748−757.

(6) Jin, Y.; Shahriari, D.; Jeon, E. J.; Park, S.; Choi, Y. S.; Back, J.; Lee, H.; Anikeeva, P.; Cho, S. W. Functional Skeletal Muscle Regeneration with Thermally Drawn Porous Fibers and Reprogrammed Muscle Progenitors for Volumetric Muscle Injury. *Adv. Mater.* **2021**, *33*, No. 2007946.

(7) Hadden, W. J.; Young, J. L.; Holle, A. W.; McFetridge, M. L.; Kim, D. Y.; Wijesinghe, P.; Taylor-Weiner, H.; Wen, J. H.; Lee, A. R.; Bieback, K.; Vo, B. N.; Sampson, D. D.; Kennedy, B. F.; Spatz, J. P.; Engler, A. J.; Choi, Y. S. Stem Cell Migration and Mechanotransduction on Linear Stiffness Gradient Hydrogels. *Proc. Natl. Acad. Sci. U.S.A.* 2017, 114, 5647−5652.

(8) Kim, Y.; Gill, E. E.; Liu, J. C. Enzymatic Crosslinking of Resilin-Based Proteins for Vascular Tissue Engineering Applications. *Biomacromolecules* 2016, 17, 2530−2539.

(9) Chen, D.; Dunker, J. P.; Losert, W.; Sarkar, S. Early Time-Point Cell Morphology Classifiers Successfully Predict Human Bone Marrow Stromal Cell Differentiation Modulated by Fiber Density in Nanofiber Scaffolds. *Biomaterials* 2021, 274, No. 120812.

(10) Kim, Y.; Kim, Y. W.; Lee, S. B.; Kang, K.; Yoon, S.; Choi, D.; Park, S. H.; Jeong, J. Hepatic Patch by Stacking Patient-Specific Liver Progenitor Cell Sheets Formed on Multiscale Electrospun Fibers Promotes Regenerative Therapy for Liver Injury. *Biomaterials* 2021, 274, No. 120899.

(11) Bao, M.; Xie, J.; Katoele, N.; Hu, X. Y.; Wang, B. X.; Piruska, A.; Huck, W. T. S. Cellular Volume and Matrix Stiffness Direct Stem Cell Behavior in a 3D Microniche. *ACS Appl. Mater. Interfaces* 2019, 11, 1754−1759.

(12) Ren, Y.; Zhang, H.; Wang, Y. P.; Du, B.; Yang, J.; Liu, L. R.; Zhang, Q. Q. Hyaluronic Acid Hydrogel with Adjustable Stiffness for Mesenchymal Stem Cell 3D Culture via Related Molecular Mechanisms to Maintain Stemness and Induce Cartilage Differentiation. *ACS Appl. Bio Mater.* 2021, 4, 2601−2613.

(13) Lin, Z. F.; Wu, M. M.; He, H. M.; Liang, Q. F.; Hu, C. S.; Zeng, Z. W.; Cheng, D. L.; Wang, G. F.; Chen, D. F.; Pan, H.B.; Ruan, C. S. 3D Printing of Mechanically Stable Calcium-Free Alginate-Based Scaffolds with Tunable Surface Charge to Enable Cell Adhesion and Facile Biofunctionalization. *Adv. Funct. Mater.* 2019, 29, No. 1808439.

(14) Hasturk, O.; Jordan, K. E.; Choi, J.; Kaplan, D. L. Enzymatically Crosslinked Silk and Silk-Gelatin Hydrogels with Tunable Gelation Kinetics, Mechanical Properties and Bioactivity for Cell Culture and Encapsulation. *Biomaterials* 2020, 232, No. 119720.

(15) Piluso, S.; Labet, M.; Zhou, C.; Seo, J. W.; Thielemans, W.; Patterson, J. Engineered Three-Dimensional Microenvironments with Starch Nanocrystals as Cell-Instructive Materials. *Biomacromolecules* 2019, 20, 3819−3830.

(16) Goldshmid, R.; Seliktar, D. Hydrogels Modulus Affects Proliferation Rate and Pluripotency of Human Mesenchymal Stem Cells Grown in Three-Dimensional Culture. *ACS Biomater. Sci. Eng.* 2017, 3, 3433−3446.

(17) Sang, Y. H.; Li, M. R.; Liu, J. J.; Yao, Y. L.; Ding, Z. Z.; Wang, L. L.; Xiao, L. Y.; Lu, Q.; Kaplan, D. L.; et al. Biomimetic Silk Scaffolds with an Amorphous Structure for Soft Tissue Engineering. *ACS Appl. Mater. Interfaces* 2018, 10, 9290−9300.

(18) Baker, B. M.; Trappmann, B.; Wang, W. Y.; Sakar, M. S.; Kim, I. L.; Shenoy, V. B.; Burdick, J. A.; Chen, C. S. Cell-Mediated Fibre Recruitment Drives Extracellular Matrix Mechanosensing In Engineered Fibrillar Microenvironments. *Nat. Mater.* 2015, 14, 1262−1268.

(19) Ye, K.; Cao, L. P.; Li, S. Y.; Yu, L.; Ding, J. D. Interplay of Matrix Stiffness and Cell-Cell Contact in Regulating Differentiation of Stem Cells. *ACS Appl. Mater. Interfaces* 2016, 8, 21903−21913.

(20) Lin, C. H.; Su, J. J. M.; Lee, S. Y.; Lin, Y. M. Stiffness Modification of Photopolymerizable Gelatin-Methacrylate Hydrogels Influences Endothelial Differentiation of Human Mesenchymal Stem Cells. *J. Tissue Eng. Regen. Med.* 2018, 12, 2099−2111.

(21) Kshitiz; Hubbi, M. E.; Ahn, E. H.; Downey, J.; Afzal, J.; Kim, D. H.; Rey, S.; Chang, C.; Kundu, A.; Semenza, G. L.; Abraham, R. M.; Levchenko, A. Matrix Rigidity Controls Endothelial Differentiation and Morphogenesis of Cardiac Precursors. *Sci. Signal.* 2012, 5, No. ra41.

(22) Wang, X.; Ding, Z. Z.; Wang, C.; Chen, X. D.; Xu, H.; Lu, Q.; Kaplan, D. L. Bioactive Silk Hydrogels with Tunable Mechanical Properties. *J. Mater. Chem. B* 2018, 6, 2739−2746.

(23) Han, H. Y.; Ning, H. Y.; Liu, S. S.; Lu, Q.; Fan, Z. H.; Lu, H. J.; Lu, G. Z.; Kaplan, D. L. Silk Biomaterials with Vascularization Capacity. *Adv. Funct. Mater.* 2016, 26, 421−436.

(24) Dupont, S.; Morsut, L.; Aragona, M.; Enzo, E.; Giulitti, S.; Cordenonsi, M.; Zanconato, F.; Digabel, J. L.; Forcato, M.; Bicciato, S.; Elvassore, N.; Piccolo, S. Role of YAP/TAZ in Mechanotransduction. *Nature* 2011, 474, 179−183.

(25) Oliver-De La Cruz, J.; Nardone, G.; Vrbsky, J.; Pompeiano, A.; Perestrelo, A. R.; Capradossi, F.; Melajová, K.; Filipensky, P.; Forte, G. Substrate Mechanics Controls Adipogenesis through YAP Phosphorylation by Dictating Cell Spreading. *Biomaterials* 2019, 205, 64−80.

(26) Chu, G.; Yuan, Z. Q.; Zhu, C. H.; Zhou, P. H.; Wang, H.; Zhang, W. D.; Cai, Y.; Zhu, X. S.; Yang, H. L.; Li, B. Substrate Stiffness- and Topography-Dependent Differentiation of Annulus Fibrosus-Derived Stem Cells is Regulated by Yes-Associated Protein. *Acta Biomater.* 2019, 92, 254−264.

(27) Xu, H.; Li, H. Y.; Ke, Q. F.; Chang, J. An Anisotropically and Heterogeneously Aligned Patterned Electrospun Scaffold with Tailored Mechanical Property and Improved Bioactivity for Vascular Tissue Engineering. *ACS Appl. Mater. Interfaces* 2015, 7, 8706−8718.

(28) Silva, C. S.; Pinto, R. D.; Amorim, S.; Pires, R. A.; Correia-Neves, M.; Reis, R. L.; Alves, N. L.; Martins, A.; Neves, N. M. Fibronectin-Functionalized Fibrous Meshes as a Substrate to Support Cultures of Thymic Epithelial Cells. *Biomacromolecules* 2020, 21, 4771−4780.

(29) Zhu, Z.; Liu, Y. H.; Xue, Y. Y.; Cheng, X. T.; Zhao, W. F.; Wang, J.; He, R.; Wan, Q. B.; Pei, X. B. Tazarotene Released from Aligned Electrospun Membrane Facilitates Cutaneous Wound Healing by Promoting Angiogenesis. *ACS Appl. Mater. Interfaces* 2019, 11, 36141−36153.

(30) Alshehri, S.; Susapto, H. H.; Hauser, C. A. E. Scaffold from Self-Assembling Tetrapeptides Support 3D Spreading, Osteogenic Differentiation, and Angiogenesis of Mesenchymal Stem Cells. *Biomacromolecules* 2021, 22, 2094−2106.

(31) Chang, B.; Ma, C.; Liu, X. H. Nanofibers Regulate Single Bone Marrow Stem Cell Osteogenesis via FAK/RhoA/YAP1 Pathway. *ACS Appl. Mater. Interfaces* 2018, 10, 33022−33031.

(32) Li, N.; Xue, F. X.; Zhang, H.; Sanyour, H. J.; Rickel, A. P.; Uttecht, A.; Fanta, B.; Hu, J. L.; Hong, Z. K. Fabrication and Characterization of Pectin Hydrogel Nanofiber Scaffolds for Differentiation of Mesenchymal Stem Cells into Vascular Cells. *ACS Biomater. Sci. Eng.* 2019, 5, 6511−6519.

(33) Wang, L. L.; Lu, G. Z.; Lu, Q.; Kaplan, D. L. Controlling Cell Behavior on Silk Nanofiber Hydrogels with Tunable Anisotropic Structures. *ACS Biomater. Sci. Eng.* 2018, 4, 933−941.

(34) Wang, K.; Liu, L. P.; Xie, J.; Shen, L.; Tao, J.; Zhu, J. T. Facile Strategy to Generate Aligned Polymer Nanofibers: Effects on Cell Adhesion. *ACS Appl. Mater. Interfaces* 2018, 10, 1566−1574.

(35) Omidinia-Anarkoli, A.; Rimal, R.; Chandorkar, Y.; Gehlen, D. B.; Rose, J. C.; Rahimi, K.; Haraszti, T.; Laporte, L. D. Solvent Induced Nanotopographies of Single Microfibers Regulate Cell Mechanotransduction. *ACS Appl. Mater. Interfaces* 2019, 11, 7671−7685.

(36) Chu, G. L.; Zhang, W. D.; Zhou, P. H.; Yuan, Z. Q.; Zhu, C. H.; Wang, H.; Li, J. Y.; Zhou, F.; Yang, Q.; Yang, H. L.; Li, B. Substrate Topography Regulates Differentiation of Annulus Fibrosus-Derived Stem Cells via CAV1-YAP-Mediated Mechanotransduction. *ACS Biomater. Sci. Eng.* 2021, 7, 862−871.

(37) Davidson, M. D.; Song, K. H.; Lee, M. H.; LIewellyn, J.; Du, Y.; Baker, B. M.; Wells, R. G.; Burdick, J. A. Engineered Fibrous Networks to Investigate the Influence of Fiber Mechanics on Myofibroblast Differentiation. *ACS Biomater. Sci. Eng.* 2019, 5, 3899−3908.

(38) Hu, X.; Xia, X. X.; Huang, S. C.; Qian, Z. G. Development of Adhesive and Conductive Resilin-Based Hydrogels for Wearable Sensors. *Biomacromolecules* 2019, 20, 3283−3293.

(39) Huang, S. C.; Qian, Z. G.; Dan, A. H.; Hu, X.; Zhou, M. L.; Xia, X. X. Rational Design and Hierarchical Assembly of a Genetically

Engineered Resilin-Silk Copolymer Results in Stiff Hydrogels. *ACS Biomater. Sci. Eng.* **2017**, *3*, 1576−1585.

(40) Song, W. W.; Qian, Z. G.; Liu, H.; Chen, H. F.; Kaplan, D. L.; Xia, X. X. On-Demand Regulation of Dual Thermosensitive Protein Hydrogels. *ACS Macro Lett.* **2021**, *10*, 395−400.

(41) Balu, R.; Dutta, N. K.; Dutta, A. K.; Choudhury, N. R. Resilin-mimetics as a Smart Biomaterial Platform for Biomedical Applications. *Nat. Commun.* **2021**, *12*, No. 149.

(42) Huang, S. C.; Fan, R. X.; Tian, K. K.; Xia, X. X.; Qian, Z. G. Controllable Fibrillization Reinforces Genetically Engineered Rubber-like Protein Hydrogels. *Biomacromolecules* **2021**, *22*, 961−970.

(43) Ng, C. P.; Hinz, B.; Swartzm, M. A. Interstitial Fluid Flow Induces Myofibroblast Differentiation and Collagen Alignment in vitro. *J. Cell Sci.* **2005**, *118*, 4731−4739.

(44) Berginski, M. E.; Gomez, S. M. The Focal Adhesion Analysis Server: A Web Tool for Analyzing Focal Adhesion Dynamics. *F1000Research* **2013**, *2*, No. 68.

(45) Lu, X. H.; Ding, Z. Z.; Xu, F. R.; Lu, Q.; Kaplan, D. L. Subtle Regulation of Scaffold Stiffness for the Optimized Control of Cell Behavior. *ACS Appl. Bio Mater.* **2019**, *2*, 3108−3119.

(46) Li, L.; Li, J. Y.; Guo, J. M.; Zhang, H. K.; Zhang, X.; Yin, C. Y.; Wang, L. M.; Zhu, Y. S.; Yao, Q. Q. 3D Molecularly Functionalized Cell-Free Biomimetic Scaffolds for Osteochondral Regeneration. *Adv. Funct. Mater.* **2019**, *29*, No. 1807356.

(47) Pei, Y.; Liu, X.; Liu, S.; Lu, Q.; Liu, J.; Kaplan, D. L.; Zhu, H. A Mild Process to Design Silk Scaffolds with Reduced β-sheet Structure and Various Topographies at the Nanometer Scale. *Acta Biomater.* **2015**, *13*, 168−176.

(48) Shin, S. R.; Jung, S. M.; Zalabany, M.; Kim, K.; Zorlutuna, P.; Kim, S. B.; Nikkhah, M.; Khabiry, M.; Azize, M.; Kong, J.; Wan, K. T.; Palacios, T.; Dokmeci, M. R.; Bae, H.; Tang, X. W.; Khademhosseini, A. Carbon-Nanotube-Embedded Hydrogel Sheets for Engineering Cardiac Constructs and Bioactuators. *ACS Nano* **2013**, *7*, 2369−2380.

(49) Zhao, D.; Cui, W.; Liu, M.; Li, J.; Sun, Y.; Shi, S.; Lin, S.; Lin, Y. Tetrahedral Framework Nucleic Acid Promotes the Treatment of Bisphosphonate-Related Osteonecrosis of the Jaws by Promoting Angiogenesis and M2 Polarization. *ACS Appl. Mater. Interfaces* **2020**, *12*, 44508−44522.

(50) Zhao, D.; Liu, M.; Li, J.; Xiao, D.; Peng, S.; He, Q.; Sun, Y.; Li, Q.; Lin, Y. Angiogenic Aptamer-Modified Tetrahedral Framework Nucleic Acid Promotes Angiogenesis In Vitro and In Vivo. *ACS Appl. Mater. Interfaces* **2021**, *13*, 29439−29449.

(51) Oswald, J.; Boxberger, S.; Jørgensen, B.; Feldmann, S.; Ehninger, G.; Bornhäuser, M.; Werner, C. Mesenchymal Stem Cells Can Be Differentiated Into Endothelial Cells In Vitro. *Stem Cells* **2004**, *22*, 377−384.

(52) Lee, J.; Henderson, K.; Massidda, M. W.; Armenta-Ochoa, M.; Im, B. G.; Veith, A.; Lee, B. K.; Kim, M.; Maceda, P.; Yoon, E.; Samarneh, L.; Wong, M.; Dunn, A. K.; Kim, J.; Baker, A. B. Mechanobiological Conditioning of Mesenchymal Stem Cells for Enhanced Vascular Regeneration. *Nat. Biomed. Eng.* **2021**, *5*, 89−102.

(53) Choi, H. J.; Zhang, H.; Park, H.; Choi, K. S.; Lee, H. W.; Agrawal, V.; Kim, Y. M.; Kwon, Y. G. Yes-Associated Protein Regulates Endothelial Cell Contact-Mediated Expression of Angiopoietin-2. *Nat. Commun.* **2015**, *6*, No. 6943.

(54) He, J.; Bao, Q. K.; Zhang, Y.; Liu, M. M.; Lv, H. Z.; Liu, Y. J.; Yao, L.; Li, B. C.; Zhang, C. H.; He, S.; Zhai, G. J.; Zhu, Y.; Liu, X.; Zhang, K.; Wang, X. J.; Zou, M. H.; Zhu, Y.; Ai, D. Yes-Associated Protein Promotes Angiogenesis via Signal Transducer and Activator of Transcription 3 in Endothelial Cells Novelty and Significance. *Circ. Res.* **2019**, *125*, No. e32.
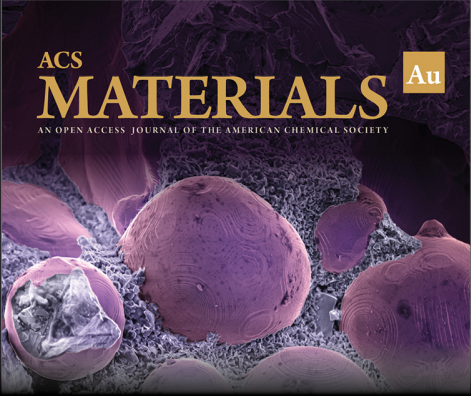
(55) Kim, J. S.; Kim, J. H.; Kim, J. Y.; Park, D. Y.; Bae, H. S.; Lee, D. H.; Kim, K. Y.; Hong, S. P.; Jang, S. P.; Kubota, Y.; Hwon, Y. G.; Lim, D. S.; Koh, G. Y. YAP/TAZ Regulates Sprouting Angiogenesis and Vascular Barrier Maturation. *J. Clin. Invest.* **2017**, *127*, 3441−3461.

(56) Lee, S.; Stanton, A. E.; Tong, X. M.; Yang, F. Hydrogels with Enhanced Protein Conjugation Efficiency Reveal Stiffness-Induced YAP Localization in Stem Cells Depends on Biochemical Cues. *Biomaterials* **2019**, *202*, 26−34.

(57) Kuroda, M.; Wada, H.; Kimura, Y.; Ueda, K.; Kioka, N. Vinculin Promotes Nuclear Localization of TAZ to Inhibit ECM Stiffness-Dependent Differentiation into Adipocytes. *J. Cell Sci.* **2017**, *130*, 989−1002.

(58) Yang, L. L.; Ge, L.; Rijn, P. V. Synergistic Effect of Cell-Derived Extracellular Matrices and Topography on Osteogenesis of Mesenchymal Stem Cells. *ACS Appl. Mater. Interfaces* **2020**, *12*, 25591−25603.

(59) Prager-Khoutorsky, M.; Lichtenstein, A.; Krishnan, R.; Rajendran, K.; Mayo, A.; Kam, Z.; Geiger, B.; Bershadsky, A. D. Fibroblast Polarization Is a Matrix-Rigidity-Dependent Process Controlled by Focal Adhesion Mechanosensing. *Nat. Cell Biol.* **2011**, *13*, 1457−1465.